applied optics

Realistic ports in integrating spheres: reflectance, transmittance, and angular redirection

Chhayly Tang,[1] Matthias Meyer,[1] Brendan L. Darby,[1] Baptiste Auguié,[1,2] and Eric C. Le Ru[1,2,*]

[1]School of Chemical and Physical Sciences, Victoria University of Wellington, P.O. Box 600, Wellington 6140, New Zealand
[2]The MacDiarmid Institute for Advanced Materials and Nanotechnology, Victoria University of Wellington, P.O. Box 600, Wellington 6140, New Zealand
*Corresponding author: eric.leru@vuw.ac.nz

Received 5 October 2017; revised 24 January 2018; accepted 25 January 2018; posted 26 January 2018 (Doc. ID 308629); published 26 February 2018

We use Monte Carlo ray-tracing modeling to follow the stochastic trajectories of rays entering a cylindrical port from inside an integrating sphere. This allows us to study and quantify properties of realistic ports of non-negligible length, as opposed to the common thin-port assumption used in most theoretical treatments, where the port is simply considered as a hole in the spherical wall. We show that most practical ports encountered in integrating sphere applications cannot be modeled as thin ports. Indeed, a substantial proportion of rays entering the port can be reflected back into the sphere, with port reflectances as high as 80% demonstrated on realistic examples. This can have significant consequences on estimates of the sphere multiplier and therefore pathlength inside the sphere, a critical parameter in many applications. Moreover, a nonzero port reflectance is inevitably associated with reduced transmittance through the port, with implications in terms of overall throughput. We also discuss angular redistribution effects in a realistic port and the consequences in terms of detected throughput within a fixed numerical aperture. Those results highlight the importance of real port effects for any quantitative predictions of optical systems using integrating spheres. We believe that those effects can be exploited to engineer ports for specific applications and improve the overall sphere performance in terms of pathlength or throughput. This work carries important implications in our theoretical understanding of integrating spheres and on the practical design of optical systems using them.

OCIS codes: (120.3150) Integrating spheres; (000.4430) Numerical approximation and analysis; (120.0120) Instrumentation, measurement, and metrology; (120.4640) Optical instruments; (080.2740) Geometric optical design; (120.3930) Metrological instrumentation.

https://doi.org/10.1364/AO.57.001581

1. INTRODUCTION

Integrating spheres, spherical cavities whose internal walls are coated with a high diffuse reflectance (HDR) material, are used in a variety of applications [1], for example diffuse reflectance spectroscopy [2–4], or gas [5–8] and liquid [9–13] absorption spectroscopy. For all those applications, one or more openings in the cavity—called ports—are necessary, typically to inject light (input port) and detect it (detection port). Rays reflect many times off the walls until they are eventually absorbed or escape via a port. The balance between these two loss mechanisms defines the properties of the integrating sphere.

The basic theory of empty integrating spheres was laid out almost 100 years ago [14–16]. The average number of wall reflections, also equal to the irradiance enhancement on the cavity wall, is called the sphere multiplier M and depends on the wall reflectivity ρ and the areas A_i of the ports (relative to total cavity wall area) [17,18],

$$M = \frac{\rho}{1 - \rho(1 - f)}, \tag{1}$$

where f denotes the total port fraction and is obtained from $f = \sum_i f_i$, with $f_i = A_i/(4\pi R^2)$ the port fraction for each port and R the sphere radius.

Implicit in this model is the assumption that all rays reaching a port escape the sphere, something which we will call the thin-port approximation. However, in many instances of integrating spheres, the cavity is milled inside a thicker block of HDR material, and ports are directly carved into the same material, as depicted schematically in Fig. 1(a). For small ports, or those with a high aspect ratio (port length over port radius), one can expect that exiting rays may hit the port wall and possibly reflect back into the sphere. As a result, one cannot assume that ports have zero reflectance, and it is therefore critical to realistically model the behavior of ports to understand the implications of those effects. This was recently pointed out

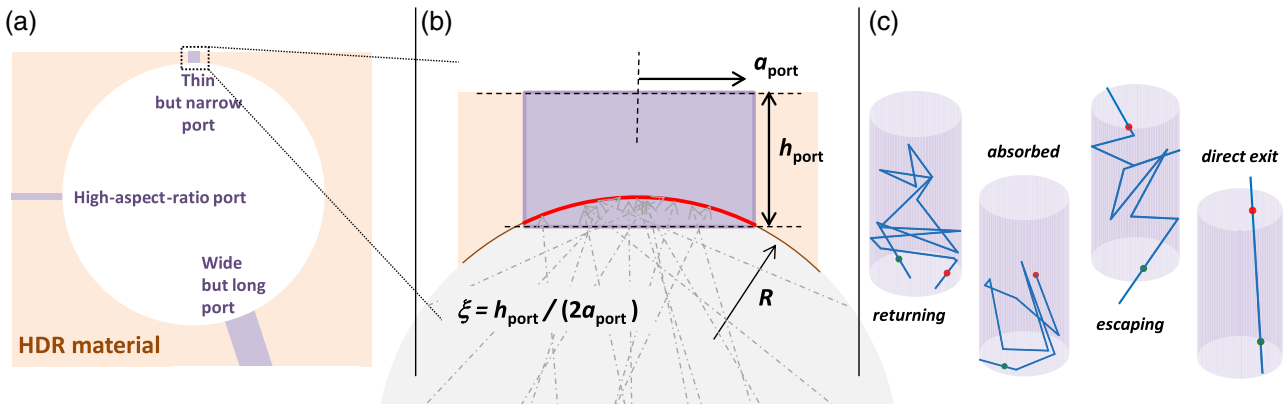

Fig. 1. (a) Schematics of representative ports in an integrating sphere where rays entering the port may hit the port wall. (b) Definition of the port geometrical parameters for the cylindrical ports considered in this work. Note that the port height is defined from the intersection of the sphere and the cylinder, not from the top of the spherical cap. Representative rays originating from inside the sphere, serving as the initial condition in the simulations, are also shown. (c) Examples of ray trajectories inside the port as obtained from Monte Carlo ray-tracing simulations. For each reflection off the wall, the rays are randomly redirected with a Lambertian profile, and have a small probability $(1 - \rho)$ of being absorbed by the wall, contributing to the port absorptance. Rays that are not absorbed either return to the sphere (contributing to a nonzero port reflectance) or escape (contributing to port transmittance).

in Ref. [19] in the context of diffuse reflectance measurements, but the authors considered only the effect of the first reflection inside the port and did not discuss how this affects the light throughput or the sphere multiplier M.

We here use Monte Carlo simulations to model the stochastic trajectories of rays inside the port and predict both reflectance and transmittance of cylindrical ports as a function of their geometrical characteristics. We study in addition how the ports affect the angular distribution of the light that is transmitted. This has important implications for many applications because light is typically collected with a limited numerical aperture (NA). We show using specific examples that those effects can have dramatic consequences on the predicted sphere multiplier and overall throughput. They must therefore be taken into account for any quantitative predictions of optical systems using integrating spheres.

2. THEORY AND NUMERICAL METHODS

Monte Carlo ray-tracing calculations were carried out to predict the properties of realistic cylindrical ports as shown schematically in Fig. 1(b). These consist in following the trajectory of a ray as it undergoes stochastic reflection/absorption events when intersecting the cavity wall [see Fig. 1(c)]. Such calculations are relatively common and have been used to understand various experimental setups involving integrating spheres [9,20–26]. We here apply them to study the trajectory of rays inside the port, not inside the integrating sphere.

A ray inside the cylindrical port is described by its position (coordinates) and direction (unit vector), and the steps in the simulation are as follows:

- Find the intersection of the trajectory with the finite cylinder defining the port. If this is located on the top (resp. bottom) face, then the ray escapes (resp. returns into the cavity).
- If the intersection is on the side wall, then we assume a Lambertian reflector of reflectivity ρ, and the ray is therefore absorbed with a probability $1 - \rho$. If not absorbed, the ray is reflected in a random direction with a Lambertian probability distribution, i.e., the angle θ with respect to the surface normal follows the probability distribution $p(\theta) = 2 \cos\theta \sin\theta$. Note that such a probability distribution results in the well-known Lambertian intensity distribution $I(\theta) \propto \cos\theta$. We here neglect the effect of any subsurface scattering or any deviation from a perfect Lambertian distribution. Note also that, although we use the same notation ρ for simplicity, the port wall reflectivity may be different to the wall reflectivity of the integrating sphere.
- The simulation continues until the ray either escapes, returns, or is absorbed.

By repeating the simulation with a large number of rays, the probability of escape τ_{port} (port transmittance), of return ρ_{port} (port reflectance), and of absorption α_{port} can be computed. Note that

$$\tau_{port} + \rho_{port} + \alpha_{port} = 1. \quad (2)$$

Those parameters depend on the wall reflectivity ρ, and on the geometric properties of the port: radius a_{port} and height h_{port} as defined in Fig. 1(b). However, since the problem is scale invariant, results will depend only on the aspect ratio, which we here define as $\xi = h_{port}/(2a_{port})$. In principle, there is also a small dependence on the angular distribution of the incoming rays (entering the port). In an ideal spherical cavity with small port fraction, the probability of receiving a ray from any other point on the sphere is uniform [18]. To account for this property, the initial characteristics of the rays are determined as follows:

- the location of the ray is chosen at random on the spherical cap defined by the intersection between the sphere and the cylindrical port [marked as a bold red line in Fig. 1(b)]; and

• the direction of the ray is chosen by picking a random point on the sphere wall outside the port and assuming that the ray originates from that point.

With this method, the angular distribution of the incoming rays entering the port is approximately what would be expected for a port in an integrating sphere. This still neglects the effect of the location of the other ports in the sphere (those effects should be negligible unless the total port fraction is large, which is uncommon). For all our simulations, we assumed a sphere radius of $R = 25a_{\text{port}}$, but the initial ray distribution has little dependence on this choice except when the ports are very wide.

For convenience, an example implementation of these simulations in Matlab/Octave is provided in Code 1, Ref. [27]. Note that this code has been simplified for readability and can therefore be readily translated to other programming languages but, as a result, is not optimized for speed.

Once the port reflectances are found, the sphere multiplier can be derived from a generalization of Eq. (1) to the case where the sphere is composed of $N+1$ regions, each of fractional area f_i and reflectance ρ_i $(i = 0 \ldots N)$, and where region 0 corresponds to where the incident light first hits the wall (for example, the sample in diffuse reflectance measurements) [28], as follows:

$$M = \frac{\rho_0}{1 - \rho\left(1 - \sum_{i=0}^{N} f_i\right) - \sum_{i=0}^{N} f_i \rho_i}. \tag{3}$$

We will here assume that light is incident on the sphere wall, not on a sample port, so that $\rho_0 = \rho$ and the expression for N ports then simplifies to

$$M = \frac{\rho}{1 - \rho(1 - f) - \sum_{i=1}^{N} f_i \rho_i}. \tag{4}$$

Note that this expression reduces to Eq. (1) within the thin-port limit (i.e., $\rho_i = 0$).

From this, the sphere throughput as detected through a given port, i.e., power exiting the port relative to power injected into the sphere, is given by

$$Q_{\text{port}} = \frac{P_{\text{port}}}{P_0} = \tau_{\text{port}} M f_{\text{port}}, \tag{5}$$

where $f_{\text{port}} = a_{\text{port}}^2/(4R^2)$ is the port fraction for a cylindrical port. This is the same expression as in the standard theory of integrating spheres [18], except that the port transmittance is explicitly included since it is no longer unity. Note also that M may be larger as the result of the nonzero port reflectances [Eq. (4)].

Finally, we will also study the angular distribution of the rays that escape the port. This may affect any experiments where a detector with a fixed NA is placed just outside the port. In the standard theory of integrating spheres (thin-port limit), the escaping rays are uniformly distributed on the port and originate from all locations on the sphere wall with equal probability. Defining θ_e as the angle of the escaping ray with respect to the cylindrical port axis, this results in a probability distribution

$$p^{\text{thin}}(\theta_e) = 2 \sin\theta_e \cos\theta_e. \tag{6}$$

For a detector of radius a_{det} and numerical aperture $\text{NA} = \sin\theta_{\text{det}}$, assuming an outcoupling efficiency of 100%, the detected throughput is then [18]

$$Q_{\text{det}}^{\text{thin}}(\text{NA}) = M f_{\text{det}} \int_0^{\theta_{\text{det}}} p(\theta_e) \mathrm{d}\theta_e = M f_{\text{det}} (\text{NA})^2, \tag{7}$$

where $f_{\text{det}} = a_{\text{det}}^2/(4R^2)$. We note that although this expression is often applied when collecting light with a fiber of a given NA, one should in principle take into account the non-negligible contribution of skew rays [29] with angles larger than strictly allowed by the fiber NA.

The detection port may be larger in practice than the detector itself, i.e., $a_{\text{det}} < a_{\text{port}}$. In the thin-port approximation, a_{port} affects only the detected throughput via its effect on M, but this may no longer be the case for realistic ports because rays may be redirected by the reflections inside the port. Using Monte Carlo simulations for a large number of rays, we can compute the histogram of θ_e for those rays that are exiting the port within the detector area and deduce $p(\theta_e)$ and Q_{det} for a realistic port.

3. RESULTS AND DISCUSSION

A. Port Reflectance and Transmittance

The results of our Monte Carlo simulations are summarized in Fig. 2, where we present the computed port reflectance, transmittance, and absorptance as a function port aspect ratio ξ, which is the most important parameter. Experimentally relevant values of ξ depend strongly on the type of applications. For example, spectroscopy typically uses smaller ports, especially if optical fibers are used, resulting in larger port aspect ratios. The sphere material is also a relevant factor, with volume scatterer such as PTFE typically requiring larger thicknesses and therefore higher ξ than near-surface scattering coatings such as barium fluoride. We also consider the effect of the port wall reflectivity ρ, with values ranging from 1 down to 0.96. The value of $\rho = 0.993$ is chosen as a typical maximum reflectivity for PTFE-based material. Those results are also tabulated in Table 1 for convenience and future reference. From those, the following conclusions can be drawn:

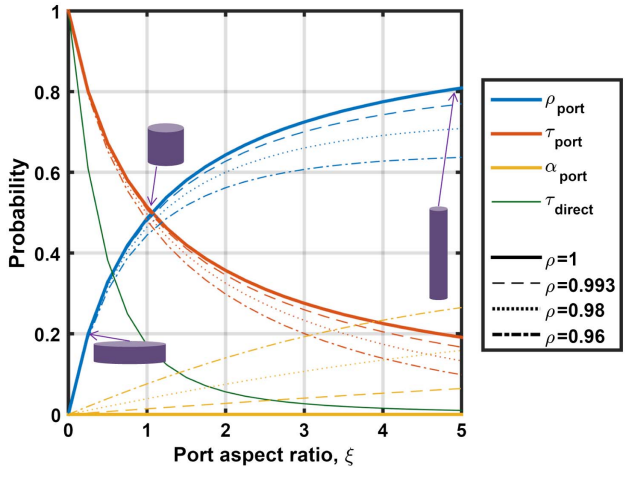

Fig. 2. Predicted port reflectance ρ_{port}, transmittance τ_{port}, and absorptance α_{port} as a function of port aspect ratio ξ for different port wall reflectivity ρ. τ_{direct} is the probability that a ray entering the port exits it without hitting the port wall. An interactive version of this figure is available online at http://nano-optics.github.io/apps/sphere.

Table 1. Predicted Port Reflectance ρ_{port}, Transmittance τ_{port}, and Absorptance α_{port} as a Function of Port Aspect Ratio $\xi = h_{port}/(2a_{port})$ for Different Wall Reflectivity ρ[a]

		$\rho = 1$			$\rho = 0.993$			$\rho = 0.98$			$\rho = 0.96$		
ξ	τ_{direct}	ρ_{port}	τ_{port}	α_{port}	ρ_{port}	τ_{port}	α_{port}	ρ_{port}	τ_{port}	α_{port}	ρ_{port}	τ_{port}	α_{port}
0.000	1.000	0.000	1.000	0.000	0.000	1.000	0.000	0.000	1.000	0.000	0.000	1.000	0.000
0.100	0.819	0.091	0.909	0.000	0.090	0.909	0.001	0.089	0.907	0.004	0.087	0.905	0.008
0.200	0.672	0.166	0.834	0.000	0.164	0.833	0.003	0.162	0.9830	0.008	0.158	0.826	0.016
0.300	0.554	0.229	0.771	0.000	0.227	0.769	0.004	0.223	0.765	0.012	0.217	0.760	0.024
0.400	0.459	0.282	0.718	0.000	0.280	0.715	0.006	0.274	0.710	0.016	0.266	0.702	0.031
0.500	0.382	0.328	0.672	0.000	0.324	0.669	0.007	0.318	0.662	0.020	0.308	0.653	0.039
0.750	0.250	0.419	0.581	0.000	0.413	0.577	0.010	0.403	0.568	0.029	0.387	0.555	0.058
1.000	0.172	0.486	0.514	0.000	0.478	0.508	0.014	0.465	0.496	0.039	0.444	0.480	0.076
1.250	0.123	0.538	0.462	0.000	0.528	0.454	0.017	0.511	0.441	0.048	0.486	0.421	0.093
1.500	0.092	0.580	0.420	0.000	0.568	0.411	0.021	0.547	0.395	0.057	0.518	0.373	0.109
1.750	0.071	0.614	0.386	0.000	0.601	0.375	0.024	0.577	0.357	0.066	0.542	0.333	0.125
2.000	0.056	0.643	0.357	0.000	0.627	0.345	0.027	0.600	0.325	0.075	0.562	0.298	0.140
2.250	0.045	0.668	0.332	0.000	0.650	0.319	0.031	0.619	0.297	0.083	0.577	0.269	0.154
2.500	0.037	0.690	0.310	0.000	0.670	0.296	0.034	0.635	0.273	0.091	0.589	0.243	0.168
2.750	0.031	0.708	0.292	0.000	0.686	0.277	0.037	0.649	0.252	0.099	0.599	0.220	0.181
3.000	0.026	0.725	0.275	0.000	0.701	0.259	0.040	0.660	0.233	0.107	0.607	0.200	0.193
3.250	0.023	0.739	0.261	0.000	0.713	0.243	0.043	0.670	0.216	0.114	0.614	0.182	0.204
3.500	0.020	0.752	0.248	0.000	0.724	0.229	0.046	0.678	0.200	0.121	0.619	0.166	0.214
3.750	0.017	0.764	0.236	0.000	0.734	0.216	0.049	0.685	0.187	0.128	0.624	0.152	0.224
4.000	0.015	0.775	0.225	0.000	0.743	0.205	0.053	0.691	0.174	0.135	0.628	0.139	0.233
4.250	0.013	0.784	0.216	0.000	0.751	0.194	0.055	0.697	0.162	0.141	0.631	0.127	0.242
4.500	0.012	0.793	0.207	0.000	0.757	0.184	0.058	0.701	0.152	0.147	0.633	0.117	0.250
4.750	0.011	0.802	0.198	0.000	0.764	0.175	0.061	0.705	0.142	0.153	0.635	0.107	0.258
5.000	0.010	0.809	0.191	0.000	0.769	0.166	0.064	0.709	0.133	0.159	0.637	0.098	0.265
10.000	0.003	0.891	0.109	0.000	0.818	0.072	0.110	0.731	0.039	0.230	0.646	0.020	0.334
20.000	0.001	0.941	0.059	0.000	0.830	0.017	0.153	0.734	0.004	0.262	0.647	0.002	0.352
30.000	0.000	0.959	0.041	0.000	0.831	0.004	0.165	0.733	0.001	0.266	0.646	0.000	0.353

[a] τ_{direct} is the probability that a ray entering the port exits it without hitting the port wall. All those quantities are computed from Monte Carlo ray tracing for 10^8 rays. The sphere radius is chosen as $R = 25a_{port}$, but the results are almost independent of R as it only slightly affects the angular distribution of the rays entering the port as long as $R \gg a_{port}$. An interactive version of this table is available online at http://nano-optics.github.io/apps/sphere.

• First and most importantly, the common thin-port assumption of $\rho_{port} = 0, \tau_{port} = 1$ is clearly inadequate over a large parameter range. Already for an aspect ratio of only $\xi = 0.25$, we predict that $\rho_{port} \approx 20\%$, and this reaches 50% for $\xi = 1$. For a typical HDR material thickness of $h_{port} = 10$ mm, the latter corresponds to a relatively wide port of 10 mm in diameter. Considering a smaller 2-mm-diameter port, the reflectance is already 50% for a port height of only $h_{port} = 2$ mm (a very thin HDR layer). For narrower and longer ports, the effect can be dramatic, with a port reflectance reaching 80% for $\xi = 5$ and $\rho \approx 1$. Such increases in reflectance are naturally accompanied by a corresponding decrease in port transmittance [see Eq. (2)] with τ_{port} as low as 10% for $\xi = 5$ and $\rho = 0.96$ for example.

• The consequences for the theoretical predictions of the sphere multiplier and sphere throughput can be significant. For example, let us consider a 50-mm-diameter sphere with $\rho = 0.993$ and two 15-mm-high, 6-mm-diameter ports (which could, for example, be used for gas spectroscopy). The standard (thin-port) theory, using $f_1 = f_2 = 0.0072$, predicts $M \approx 70$ and a throughput through one of those ports of $P_{port}/P_0 \approx 25\%$. In reality, we should instead use the real port properties for $\xi = 2.5$: $\rho_{port} \approx 0.67$ and $\tau_{port} \approx 0.3$, resulting in $M \approx 106.5$ and $P_{port}/P_0 \approx 11\%$. Such large discrepancies can have important implications when designing an integrating sphere for a particular application.

• Beyond a certain port height, the increase in reflectance saturates for $\rho < 1$, but the transmittance keeps decreasing at the expense of a larger absorption probability. The wall reflectivity ρ only has a small influence on the prediction that is more pronounced for higher ports where rays are likely to undergo more reflections before escaping or being absorbed.

These numerical results can be discussed qualitatively in simple terms. The probability of a ray hitting the port side walls increases quickly as the port becomes longer or narrower. The first reflection will more likely occur close to the port entrance. Because of the Lambertian distribution of reflections, there is a 50% chance that the rays are sent back in a direction toward the sphere. Because of the high wall reflectivity, a ray may undergo a large number of reflections before being absorbed and can therefore follow a trajectory similar to a random walk until it reaches the port exit or returns to the port entrance. For high-aspect-ratio ports, the average number of reflection becomes large, which increases the chance of being absorbed by the walls along the way, hence the increase in absorptance. We also note that the probability of a direct exit (without touching the port walls), τ_{direct}, is small compared to the overall probability of exit. τ_{direct} is related to the radiation view factor or configuration factor [30] and can be computed from our Monte Carlo simulations. As shown in Fig. 2, it decreases very sharply with aspect ratio. For a port with $\xi = 2.5$ as in the example above, the probability of direct exit is only 3.8%.

As we pointed out earlier, the nonzero port reflectance results in a higher sphere multiplier than predicted in the thin-port theory. This, however, may not translate into a higher port throughput because of the concomitant reduction in port transmittance. In fact, from a closer analysis of the formulae given above, one can see that the throughput decreases as the port aspect ratio increases. Let us, for example, consider again the simple case of a sphere with two identical ports with $f_1 = f_2 = f/2$. We then have

$$M = \frac{\rho}{1 - \rho(1 - f) - f\rho_{\text{port}}}, \tag{8}$$

which is always larger than M^{thin} when $\rho_{\text{port}} > 0$. The throughput through one of those ports can be expressed using $\rho_{\text{port}} + \tau_{\text{port}} + \alpha_{\text{port}} = 1$ as

$$Q = \frac{f}{2}\tau_{\text{port}} M = \frac{\rho f/2}{\frac{(1-\rho)(1-f)+f\alpha_{\text{port}}}{\tau_{\text{port}}} + f}. \tag{9}$$

It is clear from this expression that Q is largest when $\alpha_{\text{port}} = 0$ (as expected) and decreases as τ_{port} decreases (or as ρ_{port} increases). So, the increased port reflectance may be exploited to maximize M and therefore the pathlength inside the sphere, but this will always be at the expense of throughput.

Equation (8) can also be used to discuss in simple terms the importance of a nonzero port reflectance on M. If the total port fraction is small, namely $f \ll (1 - \rho)$, then $M \approx \rho/(1 - \rho)$, and the dominant loss mechanism is absorption in the walls. Changes in the port reflectances will have only a secondary effect on the sphere multiplier. If on the other hand the port fractions are relatively large, namely f comparable to or larger than $(1 - \rho)$, then losses through the ports are not negligible, and a change in port reflectance can have a large impact on M. Note that in all cases, the associated reduced port transmittance will have a potentially large impact on predicted throughputs.

B. Signal Collection

In the majority of applications, it is not practical to collect all the light exiting from a port. At the very least, collection is typically limited to a fixed NA. In the case where a fiber is used for collection, the probed area is also reduced to a small area around the center of the port exit, typically a disk of radius a_{det} [see inset in Fig. 3(b)]. The standard thin-port theory implicitly assumes that

- the port has a transmittance of 100% (as discussed, this is clearly wrong in most cases);
- the intensity of the light exiting the port is spatially uniform over the port area; and
- the angular distribution of the rays exiting the port is given by Eq. (6), which assumes that the Lambertian emission from the sphere of uniform radiance is not modified by the port.

One could argue that those assumptions are approximately satisfied if the optical fiber is inserted through the port with its end face located right on the sphere surface. This is, however, no longer the case if the fiber is placed at the port exit (for example, if the port is smaller than the fiber coating diameter) or if light is collected with lenses. We therefore now examine the validity of those latter two assumptions for a realistic cylindrical port, using again Monte Carlo ray-tracing simulations. For those rays that are found to escape the port, we calculate the distance to the port center when they exit, $\bar{r}$, and the exit angle θ_e with respect to the port axis. For a sufficiently large number of exiting rays (typically more than 10^5), we can study the distribution of those quantities using histograms and deduce the corresponding probability distributions $p(\bar{r})$ and $p(\theta_e)$. The results of this analysis are presented in Fig. 3 for a representative example: $\xi = 2.5$ and $\rho = 0.993$, for which $\rho_{\text{port}} = 0.67$ and $\tau_{\text{port}} = 0.30$.

$p(\bar{r})$ is compared in Fig. 3(a) to the reference distribution arising from the thin port theory: $p^{\text{thin}}(\bar{r}) = 2\bar{r}/a_{\text{port}}^2$

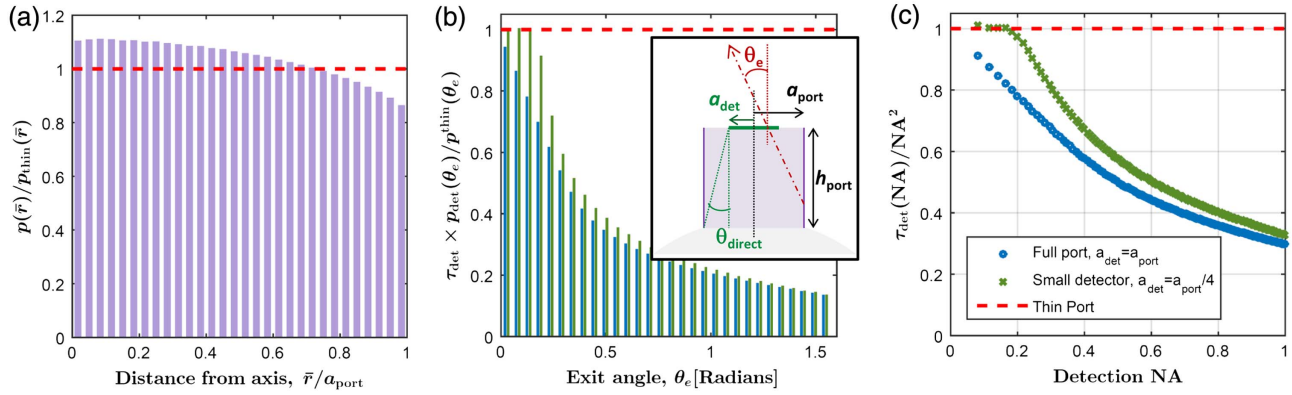

Fig. 3. Properties of rays exiting a realistic port of aspect ratio $\xi = 2.5$ with $\rho = 0.993$, computed from Monte Carlo simulation for 10^8 rays. This large number is necessary to obtain reliable statistics for detection within a reduced disk of radius $a_{\text{det}} = 0.25a_{\text{port}}$ in the port center. (a) Probability distribution of the distance from the center axis $\bar{r}$, normalized to the thin-port distribution $p^{\text{thin}}(\bar{r}) = 2\bar{r}/a_{\text{port}}^2$. (b) Probability distribution of the exit angles into a detector $p_{\text{det}}(\theta_e)$ normalized to the thin-port result $p^{\text{thin}}(\theta_e) = 2\cos\theta_e \sin\theta_e$ and weighted by the detector transmittance τ_{det} defined in Eq. (10). A value of 1 (red-dashed line) corresponds to the same probability distribution as for the rays entering the port (thin-port limit). This is computed for all rays exiting the port ($a_{\text{det}} = a_{\text{port}}$), and then only for those entering a detector of radius $a_{\text{det}} = 0.25a_{\text{port}}$, i.e., for $\bar{r} \le a_{\text{det}}$. (c) Proportion of rays detected within a given NA, either for the full port or for a detector of radius $a_{\text{det}} = 0.25a_{\text{port}}$. The power is normalized to the thin-port result and therefore takes into account the reduced transmittance of the port ($\tau_{\text{port}} = 0.30$ in this case). For $a_{\text{det}} = 0.25a_{\text{port}}$ and small NA, this low transmittance is entirely compensated by the redirection effect evidenced in (b) and to a lesser extent by the spatial redistribution evidenced in (a). As a result, the power detected within a given NA remains identical to the thin-port case up to NA ≈ 0.2.

(corresponding to uniform spatial distribution). The spatial distribution of the exiting rays is not too different from the thin-port case and remains approximately uniform. The center of the port is slightly favored compared to the periphery, but the changes are of the order of 10%–15% only and will be relevant only to the most quantitative studies. For a detecting disk of radius a_{det}, the transmittance into the detector can be defined as

$$\tau_{\mathrm{det}} = \tau_{\mathrm{port}} \left(\frac{a_{\mathrm{port}}}{a_{\mathrm{det}}}\right)^2 \int_0^{a_{\mathrm{det}}} p(\tilde{r})\mathrm{d}\tilde{r}. \quad (10)$$

The prefactor ensures that $\tau_{\mathrm{det}} = 1$ in the thin port limit. τ_{det} therefore quantifies the effect of a realistic port on the overall throughput into a detector with $a_{\mathrm{det}} \le a_{\mathrm{port}}$,

$$Q_{\mathrm{det}} = \tau_{\mathrm{det}} M f_{\mathrm{det}}, \quad (11)$$

where the detector fraction is $f_{\mathrm{det}} = a_{\mathrm{det}}^2/(4R^2)$. The distribution in Fig. 3(a) implies that τ_{det} is typically a little bit larger than τ_{port}. Note that by construction $\tau_{\mathrm{det}} = \tau_{\mathrm{port}}$ when $a_{\mathrm{det}} = a_{\mathrm{port}}$.

To study the angular distribution, we calculate $p_{\mathrm{det}}(\theta_e)$ by considering only the rays exiting the port in a disk of radius a_{det} around the center. This is shown in Fig. 3(b) for $a_{\mathrm{det}} = a_{\mathrm{port}}$ (detection over the entire port) and for $a_{\mathrm{det}} = a_{\mathrm{port}}/4$. This probability distribution also allows us to quantify the predicted port throughput within a given NA $= \sin\theta_{\mathrm{det}}$, explicitly, as follows:

$$Q_{\mathrm{det}}(\mathrm{NA}) = \tau_{\mathrm{det}} M f_{\mathrm{det}} \int_0^{\theta_{\mathrm{det}}} p_{\mathrm{det}}(\theta_e)\mathrm{d}\theta_e. \quad (12)$$

By comparison to Eq. (7), we see that $\tau_{\mathrm{det}} p_{\mathrm{det}}(\theta_e)$ quantifies the effect of the port on throughput as measured at the detector in a given direction θ_e. This is shown in Fig. 3(b), after normalization with respect to the corresponding thin-port result $p^{\mathrm{thin}}(\theta_e) = 2\cos\theta_e \sin\theta_e$. Equation (12) also leads us to define the NA-dependent transmittance into a detector of radius a_{det} and given NA, as follows:

$$\tau_{\mathrm{det}}(\mathrm{NA}) = \tau_{\mathrm{det}} \int_0^{\sin^{-1}(\mathrm{NA})} p_{\mathrm{det}}(\theta_e)\mathrm{d}\theta_e. \quad (13)$$

This quantifies the effect of the port on the throughput as measured at a detector of given NA and radius $a_{\mathrm{det}} \le a_{\mathrm{port}}$. In the thin-port limit, we simply have $\tau_{\mathrm{det}} = 1$ and $\tau_{\mathrm{det}}(\mathrm{NA}) = \mathrm{NA}^2$. The NA dependence for a realistic port normalized to this thin-port reference, $\tau_{\mathrm{det}}(\mathrm{NA})/\mathrm{NA}^2$, is plotted in Fig. 3(c) for light detected over the entire port area or limited to that of a disk of radius $a_{\mathrm{det}} = a_{\mathrm{port}}/4$.

In contrast to the spatial distribution, the angular distribution of the exiting rays is strongly changed compared to the thin-port results, with a strong angular redistribution toward the direction of the port axis. This redistribution effect is somewhat different for detection over a reduced area, i.e., if we consider only the rays exiting the port in a disk of radius $a_{\mathrm{det}} < a_{\mathrm{port}}$ around the center. An important feature of Figs. 3(b) and 3(c) is that once normalized to the total number of rays entering the detector in the thin-port limit, the probability of exit at a given angle, $\tau_{\mathrm{det}} p_{\mathrm{det}}(\theta_e)$, is always smaller than the thin-port result $p^{\mathrm{thin}}(\theta_e)$. This means that there is no net increase in the number of rays exiting at angles closer to the normal, but rather a relative decrease of those exiting at larger angles. In other words, the apparent angular redirection comes at the expense of a decrease in overall throughput, and one cannot do better than the thin-port limit in terms of throughput into a detector of given area and given NA. We believe this is related to the concept of etendue and to fundamental limits for the maximum light concentration achievable in nonimaging optics [31].

Nevertheless, Figs. 3(b) and 3(c) also show that despite the reduced overall port transmission ($\tau_{\mathrm{port}} = 0.30$), the thin-port limit throughput can be retained for detection with a fixed small NA over a reduced area. In the example of Fig. 3 and for $a_{\mathrm{det}} = a_{\mathrm{port}}/4$, the throughput is indeed unaffected by the reduced port transmission up to NA ≈ 0.2.

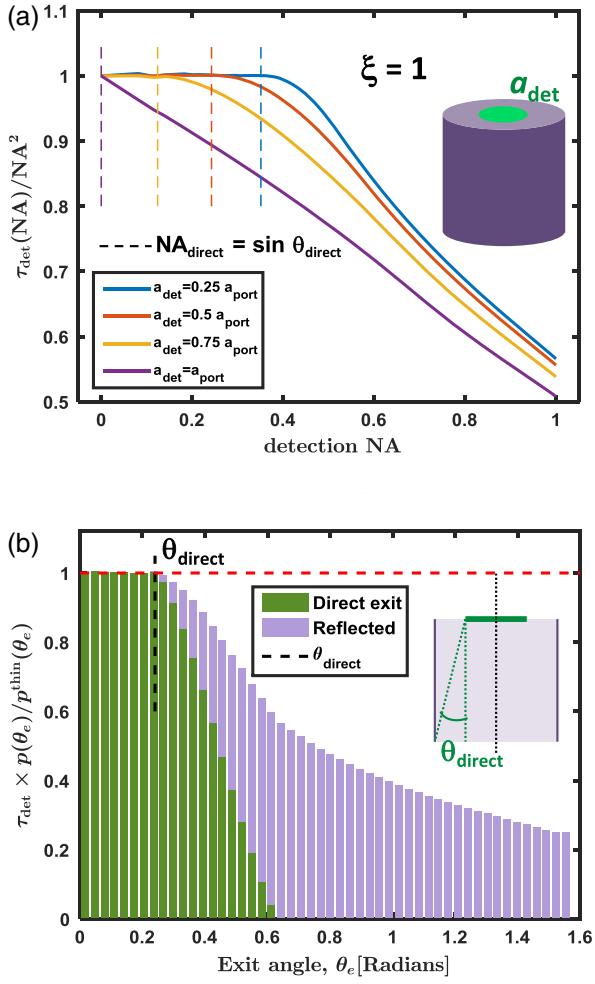

Fig. 4. (a) Proportion of rays detected within a given NA, for a detector of radius a_{det}, normalized to the thin-port result. The port has aspect ratio $\xi = 1$ and wall reflectivity $\rho = 0.993$, giving $\rho_{\mathrm{port}} = 0.48$ and $\tau_{\mathrm{port}} = 0.51$. The largest exit angle θ_{direct} for which rays can exit directly is depicted in the inset of (b) and defines $\mathrm{NA}_{\mathrm{direct}} = \sin(\theta_{\mathrm{direct}})$. Below that NA, $\tau_{\mathrm{det}}(\mathrm{NA})/\mathrm{NA}^2$ remains constant and equal to the thin port limit. (b) Probability distribution of the exit angles $p_{\mathrm{det}}(\theta_e)$ normalized to the thin-port result and weighted by detector transmittance τ_{det} for $a_{\mathrm{det}} = 0.5 a_{\mathrm{port}}$. The contribution of the rays exiting the port directly without reflecting off its wall is separated explicitly and is the only contribution for angles below $\theta_{\mathrm{direct}} = 0.24$.

To understand this result further, we carried out similar tests as a function of a_{det}, as shown in Fig. 4(a) for a port aspect ratio of $\xi = 1$ for which the effects are more visible. It is clear that the port transmittance of realistic ports remains the same as for thin ports provided one restricts the detection to an area smaller than the full port and only up to a given NA. This maximum NA increases as the port aspect ratio decreases (ultimately up to 1 for a thin port) and also increases as the detection area becomes smaller. This behavior suggests that this phenomenon is related to the rays that are exiting the port directly without reflecting off the wall. This is confirmed in Fig. 4(b) where we explicitly separate the contribution of those directly exiting rays from those that reflect at least once off the wall. We define the angle θ_{direct} and corresponding $\text{NA}_{\text{direct}} = \sin\theta_{\text{direct}}$ as shown in the inset of Fig. 4(b),

$$\theta_{\text{direct}} = \tan^{-1}\left[\frac{a_{\text{port}} - a_{\text{det}}}{h_{\text{port}}}\right] = \tan^{-1}\left[\frac{1 - a_{\text{det}}/a_{\text{port}}}{2\xi}\right],$$

$$\text{NA}_{\text{direct}} = \left[1 + \frac{4\xi^2}{(1 - a_{\text{det}}/a_{\text{port}})^2}\right]^{-\frac{1}{2}}. \quad (14)$$

One can expect from geometric arguments that all rays with exiting angle $\theta_e \le \theta_{\text{direct}}$ have traveled directly across the port, and their distribution is therefore Lambertian. This is indeed what is observed in the example presented in Fig. 4(b) where the probability distribution is exactly what would be observed for a thin port, in other words

$$\tau_{\text{det}}(\text{NA}) = \tau_{\text{det}}^{\text{thin}}(\text{NA}) = \text{NA}^2 \qquad \text{for NA} \le \text{NA}_{\text{direct}}. \quad (15)$$

Beyond θ_{direct}, rays are increasingly more likely to have reflected off the port wall and therefore potentially be sent back into the sphere, hence the drop in normalized probability distribution. When integrating this distribution up to some given NA, for example to obtain the graphs of Fig. 4(a), one then expects the overall port transmittance to follow the thin-port result until $\text{NA} \approx \text{NA}_{\text{direct}}$, as observed in Fig. 4(a).

4. CONCLUSION

In this work, we have shown that for the majority of practical cases, the standard thin-port theory of integrating spheres is inadequate. One should instead use actual values of port reflectance and port transmittance, as computed for example from Monte Carlo ray-tracing simulations. We have provided tabulated data for future reference in the common case of a cylindrical port coaxial with the sphere. In addition, we have studied and discussed the angular redistribution occurring inside a cylindrical port as a result of multiple stochastic reflections on its side walls. We have explicitly studied the experimentally relevant case of detection over a subregion of the port exit and within a given NA. We have shown that the overall port transmittance in this case is not reduced compared to the thin port theory, provided the port geometry is chosen carefully. We believe those results and associated discussions will provide practitioners with a more quantitative theory of integrating sphere pathlength and throughput, and will be invaluable in tailoring the port dimensions in integrating spheres toward specific applications such as sensing.

Funding. Royal Society of New Zealand; Rutherford Discovery Fellowship (BA).

Acknowledgment. ECLR and BA acknowledge the Royal Society of New Zealand for support via a Marsden Grant (ECLR) and a Rutherford Discovery Fellowship (BA).

REFERENCES

1. K. F. Carr, "Integrating sphere theory and applications Part II: integrating sphere applications," Surf. Coat. Int. **80**, 485–490 (1997).
2. W. W. Wendlandt and H. G. Hecht, *Reflectance Spectroscopy* (Interscience, 1966).
3. W. Erb, "Requirements for reflection standards and the measurement of their reflection values," Appl. Opt. **14**, 493–499 (1975).
4. W. R. W. Erb, "Accurate diffuse reflection measurements in the infrared spectral range," Appl. Opt. **26**, 4620–4624 (1987).
5. P. Elterman, "Integrating cavity spectroscopy," Appl. Opt. **9**, 2140–2142 (1970).
6. E. S. Fry, G. W. Kattawar, and R. M. Pope, "Integrating cavity absorption meter," Appl. Opt. **31**, 2055–2065 (1992).
7. J. T. O. Kirk, "Modeling the performance of an integrating-cavity absorption meter: theory and calculations for a spherical cavity," Appl. Opt. **34**, 4397–4408 (1995).
8. M. T. Cone, J. A. Musser, E. Figueroa, J. D. Mason, and E. S. Fry, "Diffuse reflecting material for integrating cavity spectroscopy, including ring-down spectroscopy," Appl. Opt. **54**, 334–346 (2015).
9. N. B. Nelson and B. B. Prézelin, "Calibration of an integrating sphere for determining the absorption coefficient of scattering suspensions," Appl. Opt. **32**, 6710–6717 (1993).
10. M. Babin and D. Stramski, "Light absorption by aquatic particles in the near-IR spectral region," Limnol. Oceanogr. **47**, 911–915 (2002).
11. T. Jávorfi, J. Erostyák, J. Gál, A. Buzády, L. Menczel, G. Garab, and K. R. Naqvi, "Quantitative spectrophotometry using integrating cavities," J. Photochem. Photobiol. B **82**, 127–131 (2006).
12. A. K. Gaigalas, H.-J. He, and L. Wang, "Measurement of absorption and scattering with an integrating sphere detector: application to microalgae," J. Res. Natl. Inst. Stand. Technol. **114**, 69–81 (2009).
13. B. L. Darby, B. Auguié, M. Meyer, A. E. Pantoja, and E. C. Le Ru, "Modified optical absorption of molecules on metallic nanoparticles at sub-monolayer coverage," Nat. Photonics **10**, 40–45 (2016).
14. A. H. Taylor, "The measurement of diffuse reflection factors and a new absolute reflectometer," J. Opt. Soc. Am. **4**, 9–23 (1920).
15. F. A. Benford, "An absolute method for determining coefficients of diffuse reflection," Gen. Electr. Rev. **23**, 72–75 (1920).
16. C. H. Sharp and W. F. Little, "Measurements of reflection factors," Trans. Illum. Eng. Soc. **15**, 802–810 (1920).
17. J. A. Jacquez and H. F. Kuppenheim, "Theory of the integrating sphere," J. Opt. Soc. Am. **45**, 460–470 (1955).
18. K. F. Carr, "Integrating sphere theory and applications Part I: integrating sphere theory and design," Surf. Coat. Int. **80**, 380–385 (1997).
19. J. Hwang, H. Cho, D.-J. Shin, and K. L. Jeong, "Correction of port reflection effect for integrating sphere-based reflection measurements," Metrologia **50**, 472–481 (2013).
20. B. Li, X. Yu, and L. Liu, "Backward Monte Carlo simulation for apparent directional emissivity of non-isothermal semitransparent slab," J. Quant. Spectrosc. Radiat. Transfer **91**, 173–179 (2005).
21. S. K. Wan and Z. Guo, "Correlative studies in optical reflectance measurements of cerebral blood oxygenation," J. Quant. Spectrosc. Radiat. Transfer **98**, 189–201 (2006).
22. H. Parviainen and K. Muinonen, "Bidirectional reflectance of rough particulate media: ray-tracing solution," J. Quant. Spectrosc. Radiat. Transfer **110**, 1418–1440 (2009).
23. C. Xiong and J. Shi, "Simulating polarized light scattering in terrestrial snow based on bicontinuous random medium and Monte Carlo ray tracing," J. Quant. Spectrosc. Radiat. Transfer **133**, 177–189 (2014).
24. J. Zhao, J. Tan, and L. Liu, "Monte Carlo method for polarized radiative transfer in gradient-index media," J. Quant. Spectrosc. Radiat. Transfer **152**, 114–126 (2015).

25. B. Liu, Y. Yuan, Z.-Y. Yu, X. Huang, and H.-P. Tan, "Numerical investigation of measurement error of the integrating sphere based on the Monte-Carlo method," Infrared Phys. Technol. **79**, 121–127 (2016).
26. Y. Villanueva, C. Veenstra, and W. Steenbergen, "Measuring absorption coefficient of scattering liquids using a tube inside an integrating sphere," Appl. Opt. **55**, 3030–3038 (2016).
27. C. Tang, M. Meyer, B. L. Darby, B. Auguie, and E. C. Le Ru, "Matlab/Octave script. Simplified code for calculating port reflectance and transmittance," figshare, 2018, https://doi.org/10.6084/m9.figshare.5471770.
28. D. G. Goebel, "Generalized integrating-sphere theory," Appl. Opt. **6**, 125–128 (1967).
29. A. W. Snyder and J. D. Love, *Optical Waveguide Theory* (Chapman & Hall, 1983).
30. B. T. F. Chung and M. H. N. Naraghif, "Some exact solutions for radiation view factors from spheres," AIAA J. **19**, 1077–1081 (1981).
31. I. M. Bassett, W. T. Welford, and R. Winston, "Nonimaging optics for flux concentration," in *Progress in Optics*, E. Wolf, ed. (Elsevier, 1989), Vol. **27**, pp. 161–226.